Astron. Nachr. / AN **337**, No. 10, 1090 – 1098 (2016) / **DOI** 10.1002/asna.201612447

Flow and magnetic field properties in the trailing sunspots of active region NOAA 12396

M. Verma[1,⋆], **C. Denker**[1], **F. Böhm**[1,2], **H. Balthasar**[1], **C. E. Fischer**[3], **C. Kuckein**[1], **N. Bello González**[3], **T. Berkefeld**[3], **M. Collados**[4], **A. Diercke**[1,5], **A. Feller**[6], **S.J. González Manrique**[1,5], **A. Hofmann**[1], **A. Lagg**[6], **H. Nicklas**[7], **D. Orozco Suárez**[12], **A. Pator Yabar**[4,8], **R. Rezaei**[4], **R. Schlichenmaier**[3], **D. Schmidt**[9], **W. Schmidt**[3], **M. Sigwarth**[3], **M. Sobotka**[10], **S.K. Solanki**[6,11], **D. Soltau**[3], **J. Staude**[1], **K.G. Strassmeier**[1], **R. Volkmer**[3], **O. von der Lühe**[3], and **T. Waldmann**[3]

[1] Leibniz-Institut für Astrophysik (AIP), An der Sternwarte 16, 14482 Potsdam, Germany
[2] Humboldt-Universität zu Berlin, Institut für Physik, Newtonstraße 15, 12489 Berlin, Germany
[3] Kiepenheuer-Institut für Sonnenphysik, Schöneckstr. 6, 79104 Freiburg, Germany
[4] Instituto de Astrofísica de Canarias, C/ Vía Láctea s/n, 38205 La Laguna, Tenerife, Spain
[5] Universität Potsdam, Institut für Physik und Astronomie, Karl-Liebknecht-Straße 24/25, 14476 Potsdam, Germany
[6] Max-Planck-Institut für Sonnensystemforschung, Justus-von-Liebig-Weg 3, 37077 Göttingen, Germany
[7] Institut für Astrophysik, Georg-August-Universität Göttingen, Friedrich-Hund-Platz 1, 37077 Göttingen, Germany
[8] Departemento de Astrofísica, Universidad de La Laguna, 38205 La Laguna, Tenerife, Spain
[9] National Solar Observatory, 3010 Coronal Loop, Sunspot, NM 88349, USA
[10] Astronomical Institute, Academy of Sciences of the Czech Republic, Fričova 298, 25165 Ondřejov, Czech Republic
[11] School of Space Research, Kyung Hee University,Yongin, Gyeonggi-Do, 446-701, Republic of Korea
[12] Instituto de Astrofísica de Andalucía, Glorieta de la Astronoma, 18008 Granada, Spain

Received 2016 Jul 16, accepted 2016 Sep 30
Published online 2016 Dec 02

Key words Sun: magnetic fields – sunspots – methods: data analysis – techniques: polarimetric – techniques: spectroscopic

Improved measurements of the photospheric and chromospheric three-dimensional magnetic and flow fields are crucial for a precise determination of the origin and evolution of active regions. We present an illustrative sample of multi-instrument data acquired during a two-week coordinated observing campaign in August 2015 involving, among others, the GREGOR solar telescope (imaging and near-infrared spectroscopy) and the space missions Solar Dynamics Observatory (SDO) and Interface Region Imaging Spectrograph (IRIS). The observations focused on the trailing part of active region NOAA 12396 with complex polarity inversion lines and strong intrusions of opposite polarity flux. The GREGOR Infrared Spectrograph (GRIS) provided Stokes $IQUV$ spectral profiles in the photospheric Si I λ1082.7 nm line, the chromospheric He I λ1083.0 nm triplet, and the photospheric Ca I λ1083.9 nm line. Carefully calibrated GRIS scans of the active region provided maps of Doppler velocity and magnetic field at different atmospheric heights. We compare quick-look maps with those obtained with the "Stokes Inversions based on Response functions" (SIR) code, which furnishes deeper insight into the magnetic properties of the region. We find supporting evidence that newly emerging flux and intruding opposite polarity flux are hampering the formation of penumbrae, i.e., a penumbra fully surrounding a sunspot is only expected after cessation of flux emergence in proximity to the sunspots.

1 Introduction

Sunspots are the most prominent magnetic features on the solar surface. However, the detailed physics behind many facets of sunspot magnetic and flow structures still need a better understanding – starting with global phenomena like the moat flow (Brickhouse & Labonte 1988) and Evershed effect (Evershed 1909) all the way to local magnetic field and flow properties encountered in individual penumbral filaments (e.g., Scharmer et al. 2002). The advancement of observing facilities is providing us nowadays with the fine details of flow and magnetic structures in and around sunspots.

The radial outward motions in the sunspot penumbra at photospheric levels are reversed in the chromosphere with material flowing towards the umbra. This inverse Evershed effect was already seen by Evershed (1909). In addition, the radial velocities are increased from photosphere to transition region (Dere et al. 1990). Recently, Tiwari et al. (2015) studied the global magnetic and flow properties of a sunspot and their depth dependency. They find upflows at photospheric level in the inner penumbra and downflows in the outer penumbra, which continues beyond the visible boundary of the penumbra, thus corroborating previous studies

⋆ Corresponding author: mverma@aip.de

(e.g., Rimmele 1995; Rimmele & Marino 2006; Tritschler et al. 2004; Westendorp Plaza et al. 1997).

Schlichenmaier et al. (1998a,b) presented a model for the penumbral fine structure and the Evershed effect in sunspots. In their simulation, a magnetic flux tube is placed inside a monolithic sunspot just at the magnetopause, i.e., transition to the surrounding quiet Sun. The tube becomes buoyant because of radiative heat exchange between the tube and the adjacent quiet Sun. Hence, the tube starts to rise through the subphotospheric penumbra. Schlichenmaier (2002) presented an updated version of the moving flux tube model, where he explored the time dependent nature of a thin magnetic flux tube embedded in the penumbra. As in earlier siphon model (see Montesinos & Thomas 1997, for a recent version) the moving flux tube model reproduced the Evershed flow. Alternatively, Spruit & Scharmer (2006) proposed a gappy penumbral model explaining the fine structure, heating, and magnetic field of penumbrae. According to them penumbral filaments correspond to field-free gaps inside the sunspot's potential field, where convection brings up hot plasma from below.

The first evidence of magnetic fields in sunspots was reported by Hale (1908), and a detailed description of their discovery is given by Del Toro Iniesta (1996). Absorption lines in the visible and the near-infrared are usually used to measure the photospheric magnetic fields of sunspots. The many aspects of sunspot magnetic fields, starting from global properties to their small scale structure, are discussed in the reviews by Solanki (2003) and more recently by Borrero & Ichimoto (2011).

Schlichenmaier et al. (2010a,b) and Rezaei et al. (2012) presented observations of the formation of a sunspot penumbra. They found that ongoing flux emergence in the vicinity of the sunspot prevented the formation of a stable penumbra. The umbral area remained constant while the penumbra developed. Rezaei et al. (2012) observed small flux patches associated with elongated granules and concluded that they are the building blocks leading to the formation of active regions. Balthasar et al. (2013) presented the magnetic properties of a decaying sunspot. In the proximity of the spot, they found a chromospheric location with strong downflows but without a photospheric counterpart. The magnetohydrodynamic (MHD) simulations of Cheung et al. (2010) and Rempel & Cheung (2014) are able to reproduce many of the observational properties of active regions starting from flux emergence, to the evolution of the buoyant flux tubes, and ultimately to their decay. Thus, the combination of high-resolution observations and simulations is the key to an improved understanding of fundamental processes on the Sun.

In this study, we present a small portion of a data set taken during a two-week coordinated observing campaign with GREGOR, SDO, IRIS, VTT, and HINODE (the last two are not included in this study), which focused on the trailing sunspots in active region NOAA 12396 on 2015 August 6. The observations and data reduction are described in Sect. 2. The temporal evolution of the region along with the velocity and magnetic properties are presented in Sect. 3, which is followed by a summary of this study in the conclusions (Sect. 4).

2 Observations and data reduction

The aim of the coordinated observing campaign was to obtain high-resolution observations and accurate measurements of the photospheric and chromospheric three-dimensional magnetic and flow fields around active region filaments. However, due to Saharan dust incursion called "Calima" (see Fig. 11 in Brandt & Wöhl 1982) and unfavorable seeing conditions, observations were carried out only on a few days – the best and most complete data are discussed in the following.

2.1 Observations

Active region NOAA 12396 appeared as bright plage on the east limb on 2015 August 3. It started to grow and produced several pores by August 4. The leading sunspot with a light-bridge was established by August 5 with the trailing part being in the formation process. On August 6, the day of the GREGOR observations, the trailing part comprised three sunspots with rudimentary penumbrae and a few mixed polarity pores. It was classified as $\beta\gamma/\beta$, i.e., the region was bipolar with a complex magnetic neutral line. The region continued to grow until August 10. It started its declining phase by August 11 and simplified significantly thereafter. However, the leading sunspot remained intact, even very close to the west limb. The region was predicted to have M-class flares, but it never reached this level of activity producing only multiple C-class flares (see SolarMonitor, Gallagher et al. 2002).

The trailing sunspots of the region were observed with GRIS (Collados et al. 2007, 2012) at the 1.5-m GREGOR solar telescope (Denker et al. 2012; Schmidt et al. 2012) on 2015 August 6 starting at 09:24 UT. The instrument covered the He I λ1083.0 nm spectral region recording spectropolarimetric data. The spectral window of about 1.832 nm includes the photospheric Si I λ1082.7 nm line, the chromospheric He I λ1083.0 nm triplet, and the photospheric Ca I λ1083.9 nm line as well as many telluric lines. The number of spectral points was $n = 1010$, and the spectral sampling was 1.81 pm pixel^{-1}. The scan covered 43.2″ in 300 steps with a step size of about 0.144″. The image scale along the slit was about 0.136″ pixel^{-1} resulting in a field-of-view (FOV) of about 62″×43″. GRIS is a dual beam polarimeter with four modulation states. In each modulation state 10 accumulations were taken with 100 ms exposure time. With these setting it took 30 min for one scan of the sunspots.

The observed Si I line is a strong photospheric absorption line at λ1082.7 nm. It originates from the transition between the $4s\,^3P_2$ and $4p\,^3P_2$ levels with a Landé factor

$g_{\rm eff}$ = 1.5, whereas the He I triplet forms in the upper chromosphere (Avrett et al. 1994). It originates from three transitions between the lower $2s\,^3S_1$ and upper $2p\,^3P_{2,1,0}$ levels (Swensson et al. 1970). Although three lines belong to the triplet, only two components can be observed because two lines occupy the same position in the spectrum. The two blended lines at λ1083.030 nm and λ1083.025 nm are called the "red" component, and the unblended line at λ1082.909 nm is called the "blue" component (Trujillo Bueno et al. 2002). Apart from the Si and He spectral lines, we observe the photospheric Ca I line at λ1083.9 nm. This line results from the transition between $4p\,^3P_2$ and $3d\,^3P_2$ levels, and it is also magnetically sensitive with a Landé factor $g_{\rm eff}$ = 1.5 (Swensson et al. 1970). All three magnetically sensitive lines provide information about the magnetic field and its coupling between the photosphere and chromosphere (e.g., Kuckein et al. 2012; Rüedi et al. 1995).

We used SDO (Scherrer et al. 2012) to provide context information for the high-resolution observations. A full-disk continuum image and a line-of-sight (LOS) magnetogram of the Helioseismic and Magnetic Imager (HMI, Couvidat et al. 2012; Schou et al. 2012; Wachter et al. 2012) along with an Fe IX λ17.1 nm EUV image and a λ160 nm FUV image of the Atmospheric Imaging Assembly (AIA, Lemen et al. 2012) present an overview of active region NOAA 12396 (Fig. 1). The black and white rectangular boxes indicate the FOV observed by GRIS. In addition, we downloaded continuum images and LOS magnetograms every hour from 2015 August 6–14 to follow the photospheric evolution of the active region.

Along with SDO we used IRIS high-resolution slit-jaw images (De Pontieu et al. 2014) of the transition region captured in the C II λ133 nm, Si IV λ140 nm, Mg II k λ279.6 nm channels and a continuum image at λ283.2 nm as additional context information. Since the IRIS observations were not simultaneously taken with the GREGOR observations, data are only available from a few hours earlier. Sixteen images per channel were recorded with a cadence of 68 s on 2015 August 6 starting at 06:30 UT. The FOV of slit-jaw images is 119″×119″. We created a collage of 16 images to show a much larger FOV covering the entire active region as shown in Fig. 2.

2.2 Data reduction

The basic GRIS data reduction is carried out on-site using the GRIS data pipeline (Collados, priv. communication). The various steps include dark subtraction, flat-field correction, calibration of telescope and instrument, and residual crosstalk removal (Collados 1999; Schlichenmaier & Collados 2002). At GRIS, the latter correction is only applied for crosstalk from I to (Q, U, V) by forcing the (Q, U, V) continuum to zero. No correction is applied for the residual crosstalk from (Q, U, V) to (Q, U, V). For flat-field correction, a quiet-Sun region near the solar disk center was scanned with 15 scan steps and 10 accumulations while the telescope was continuously moving in both axes. The calibration of telescope and instrument utilizes the GREGOR polarimetric calibration unit (GPU, Hofmann et al. 2012), which conditions the incident beam of light in a known polarization state, so that the response of the polarimeter can be calculated. The measurement of the Stokes parameters is affected by "seeing-induced'' crosstalk. This means that temporal variations of the parameters at scales below 0.5 s lead to false polarization signals. As described in Collados et al. (2007, 2012), the polarimeter splits the light into two beams of opposite polarity, which are finally combined to reduce this crosstalk. However, a certain amount of residual crosstalk remains in the combined beams.

The GRIS wavelength calibration relies on a comparison of the observed profiles with a near-infrared atlas profile obtained with the Fourier Transform Spectrometer (FTS) of the McMath-Pierce solar telescope at the Kitt Peak National Observatory (Wallace et al. 1996). The continuum of the observed spectrum is not a constant but shows an intensity variation. This variation is corrected by comparing observed and atlas spectra, focusing only on the continuum, i.e., excluding the spectral lines. The intensity variation is decomposed into its Fourier components and restored for entire spectral region using just eleven coefficients. Dividing the observed spectrum by this profile results in a spectrum with a constant continuum level, which was then normalized to unity.

To correct variations in the sky transparency, changes in the intensity over time were examined. For this purpose, we used a quiet-Sun mask and computed an average value for the intensity of granulation for all slit positions. This average profile was smoothed using again Fourier decomposition and restoration analogously to the intensity variation profile but this time with only nine coefficients. The observed profiles were divided by this smoothed profile to correct variations in sky transparency. Drifts of the spectrograph over the day also affect GRIS profiles. Telluric lines were used to estimate these drifts. The difference between line-core and mean position was averaged in the slit direction, yielding a velocity representing the spectrograph drift for every scan. The spectrograph drift was in the range −100 to +300 m s^{-1}. The spectra were interpolated to the correct spectral range effectively removing the spectrograph drift. For the wavelength calibration and dispersion computation we used the flat-field scans taken at the disk center. We used a parabola fit to the Si I λ1082.7 nm and Ca I λ1083.9 nm line cores to obtain the central wavelength. We carefully matched the observed spectral profile to the one extracted from the Kitt Peak near-infrared FTS atlas.

3 Results

3.1 Temporal evolution of the region

The SDO (Fig. 1) and IRIS (Fig. 2) images provide an overview of active region NOAA 12396. The IRIS images,

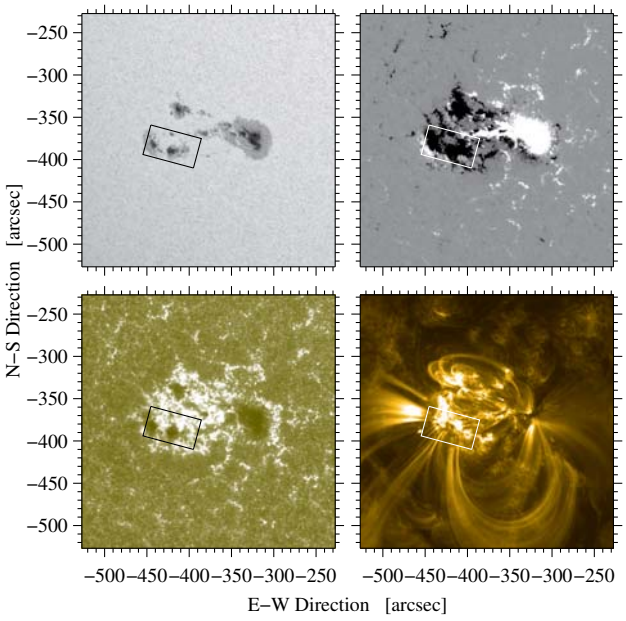

Fig. 1 Overview of active region NOAA 12396: HMI continuum image (*top-left*), HMI magnetogram (*top-right*), AIA λ160 nm (*bottom-left*), and AIA Fe IX λ17.1 nm image (*bottom-right*) as observed at 08:40 UT on 2015 August 6. The rectangle is the FOV covered by GRIS.

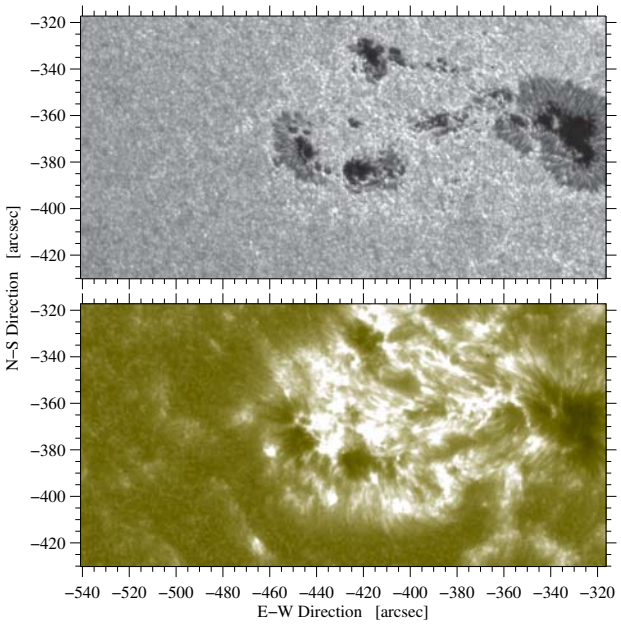

Fig. 2 Collage of IRIS slit-jaw images in the λ283.2 nm (*top*) and λ279.6 nm (*bottom*) passbands, covering most of active region NOAA 12396, which was observed at 06:30 UT on 2015 August 6. These images in Mg II h & k passband are excellent probes of lower and upper chromosphere.

observed a few hours before the GRIS observations, contain the leading sunspot with a light-bridge along with the three trailing sunspots. The region between leading and trailing sunspots includes many mixed-polarity pores as seen in the IRIS λ283.2 nm continuum image. Brightenings are visible at this location in the IRIS λ279.6 nm image. In addition, small brightenings can be seen at the edges of the trailing sunspots, e.g., at (−435″, −400″) and (−460″, −380″). On visual inspection, the brightenings in the IRIS λ279.6 nm image match the brightenings in the AIA λ160 nm image (see Fig. 1). Furthermore, filamentary structures as seen in the IRIS λ279.6 nm image, extending beyond the photometric boundary of the sunspot penumbra are present around the sunspots.

The SDO images and magnetograms provide us with the temporal evolution of the region before and after the GREGOR observations. The continuum images and magnetograms in Fig. 3 start at 20:00 UT on August 5 and end at 22:00 UT on August 6. They were organized in increasingly larger time intervals (2, 4, and 8 hours) centered on the high-resolution GRIS observations. A region-of-interest (ROI) of 126″×126″ was selected covering all three trailing sunspots. In the continuum image at 20:00 UT on 2016 August 5 all three spots are present. The spots are marked as S1, S2, and S3 to aid their identification and simplify the discussion. Spot S1 has an irregular penumbra, and its umbra contains a light-bridge, whereas spots S2 and S3 are collections of pores. All three spots are of negative polarity. There is an intrusion of positive polarity in the right side of the ROI, which belongs to the leading sunspot of the active region. The central part of the ROI is filled with mixed-polarity pores.

After eight hours, spots S2 and S3 have stronger umbrae. Spot S2 also developed an irregular penumbra, whereas the umbra of spot S3 has a light-bridge. The positive polarity intrusion is extended and seems to grow in area. A small negative polarity pore starts to appear in the center of the ROI in the region between spots S1/S2 and S3 (60″, 50″). In next four hours, the light-bridge in spot S1 disappeared and its penumbral area increased. The rudimentary penumbra of spot S2 is slightly elongated towards the leading sunspot. Over next two hours (at 10:00 UT), for both spots S1 and S2 the penumbrae never fully developed to encircle the whole spots. A penumbra never establishes in the direction facing the constantly changing central part of the ROI. As seen in the magnetograms and continuum images, this region is a site of ongoing flux emergence. No steady penumbra is formed during this flux emergence, which is consistent with the suppression of penumbral formation by flux emergence as shown by Schlichenmaier et al. (2010b) and Romano et al. (2013).

Between 14:00 UT and 22:00 UT, the penumbra of spot S3 fully surrounds the spot. However, towards the end of August 6 at 22:00 UT the S3 penumbra pointing towards the central inner region disintegrates. Two new features appear above the central pore. This pore and the surrounding features later developed into a sunspot (not shown in Fig. 3). These observations suggest that the sunspot was created by advection of smaller magnetic flux elements. By the end of August 6 the gap between spots S1 and S2 be-

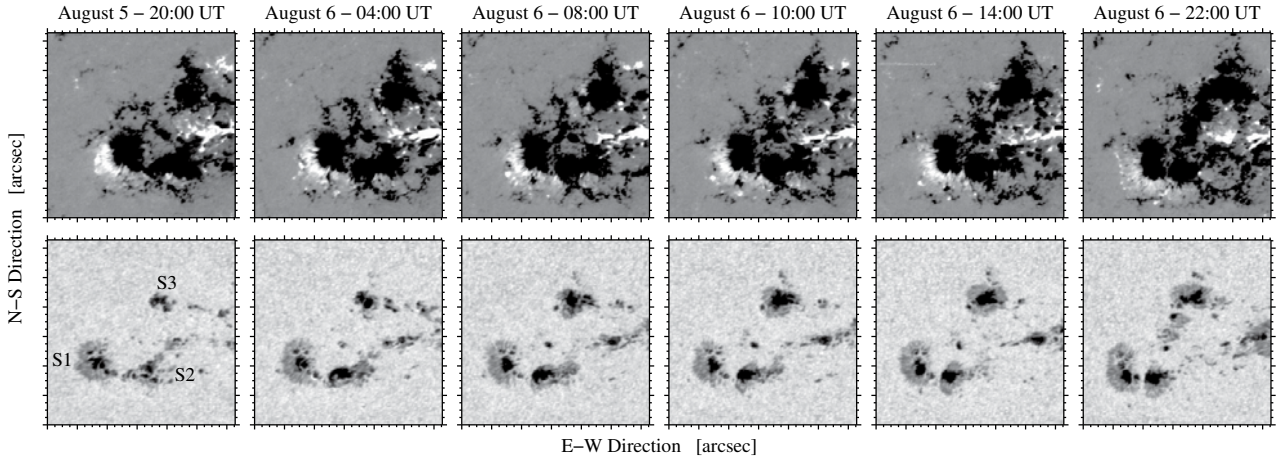

Fig. 3 Trailing sunspots of active region NOAA 12396 as observed by SDO. Details of HMI full-disk magnetograms and continuum images (126″×126″) show the temporal evolution of the region starting at 20:00 UT on August 5 until 22:00 UT on August 6. The time interval between the cutouts are 8, 4, 2, 4, and 8 hours, respectively. The magnetograms are displayed between ±250 G. Major tick marks are separated by 20″.

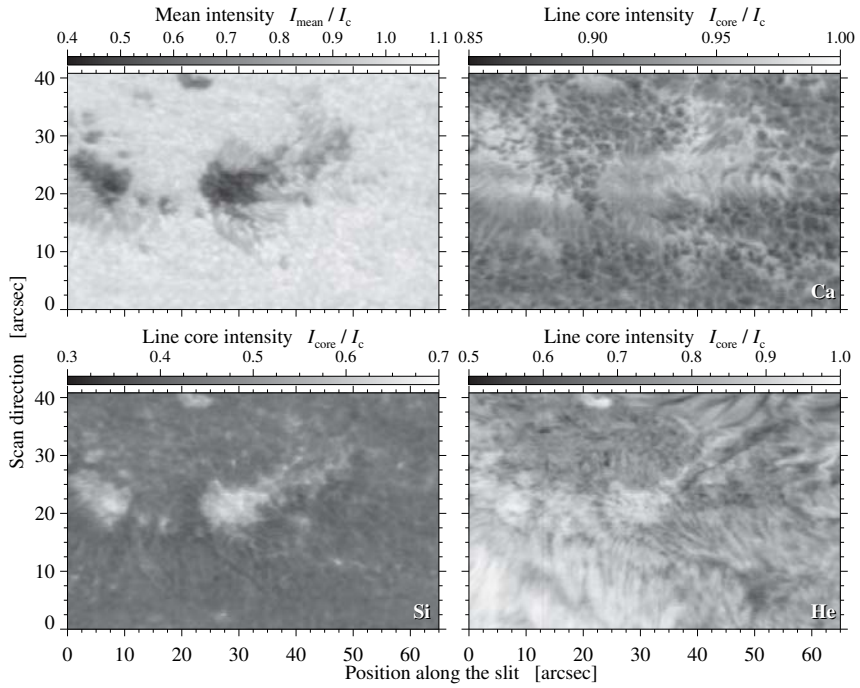

Fig. 4 Slit-reconstructed GRIS images of the mean continuum intensity (*top-left*) and the line core intensities for the Ca I line (*top-right*), the Si I line (*bottom-left*), and the He I triplet (*bottom-right*).

comes smaller. The positive polarity intrusion survives over the whole day. However, it seems to split as is evident in the magnetogram taken at 22:00 UT. One part merges with the leading sunspot, and the other becomes part of the mixed-polarity region between leading and trailing spots.

3.2 Line core intensity and velocity

The GRIS spectra offer us the opportunity to infer physical properties of the solar atmosphere. The processed profiles are used for further analysis. We focus on the Si I λ1082.7 nm line, the red component of He I triplet at λ1083.03 nm, and the Ca I λ1083.9 nm line. We refer to these lines as Si I, He I, and Ca I throughout the paper. The LOS velocities for the spectral lines were calculated using the Fourier phase method (Schmidt et al. 1999), which measures the center-of-gravity of a given spectral line. The intensities at the line core position were determined by a parabola fit to the line core.

Figure 4 shows the line core intensity maps for all the three lines along with the mean continuum intensity map. In the continuum map only spots S1 and S2 are visible along with the central pore. Both spots have irregular penumbrae. The Ca I and Si I lines are shallower in the presence of strong magnetic fields. In the map for the Ca I line core intensity, which originates from the lower photosphere, we see clearly the granulation pattern. This is an indication of very good seeing conditions during the scan. Granulation is also ev-

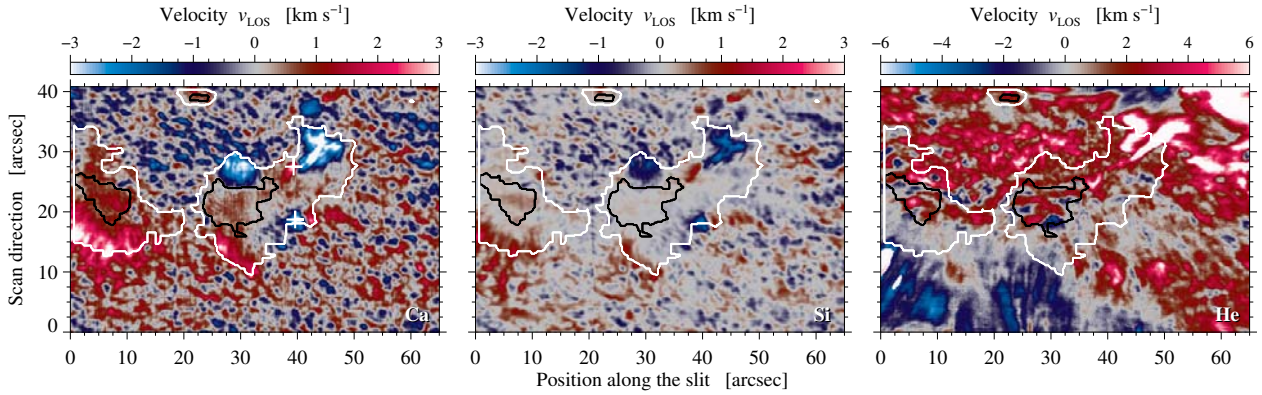

Fig. 5 GRIS slit-reconstructed maps of the LOS velocities for the Ca I (*left*), Si I (*middle*), and He I (*right*) spectral lines observed at 09:24 UT on 2015 August 6. These velocities were inferred using the very robust center-of-gravity method. The white "+" signs mark the locations of up- and downflows for which observed and fitted Stokes profiles are shown in Fig. 7. The black contours mark the umbra-penumbra boundaries, whereas the white contours mark the penumbra-granulation boundaries.

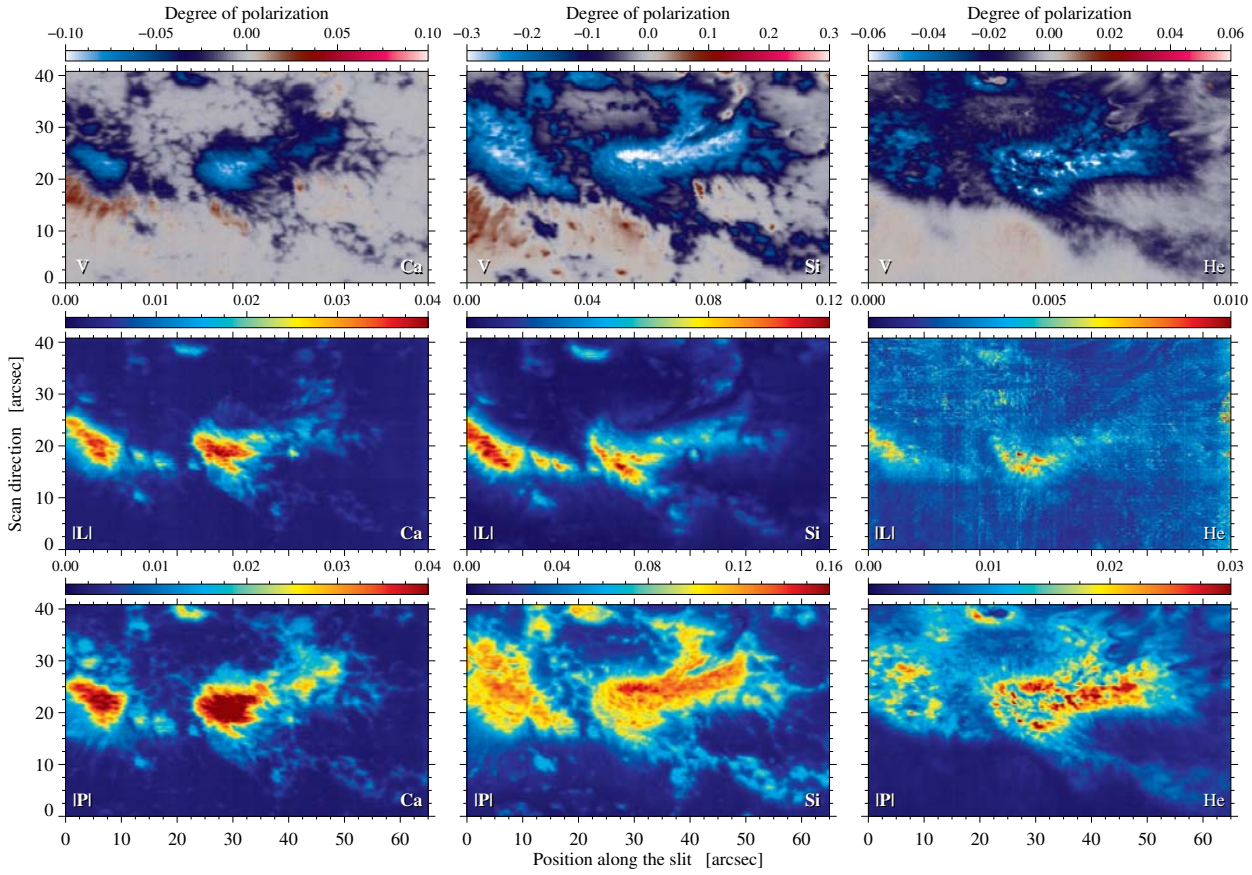

Fig. 6 Slit-reconstructed "quick-look" maps of signed Stokes V, total linear polarization $|L|$, and total polarization $|P|$ (*top to bottom*) for the Ca I, Si I, and He I spectral lines (*left to right*) obtained with GRIS starting at 09:24 UT on 2015 August 6.

ident in Si I line core intensity map, although it is not as clearly defined, which is expected for a spectral line originating in the upper photosphere. Predictably, in the He I line, which represents chromospheric layers, the line core intensity map is void of any signature of granulation. However, it contains a few thin filamentary structures, e.g., at coordinates (40″, 40″). The He I line core intensity approaches the quiet-Sun continuum intensity in the lower left corner of the ROI.

Apart from line core intensity maps, we also computed LOS velocities for all three lines as compiled in Fig. 5. While creating these maps, the average photospheric velocity of the quiet Sun, as measured in the Ca I line, was used as the reference velocity. In the LOS velocity map of the Ca I line, similar to its line core map, the granulation pattern

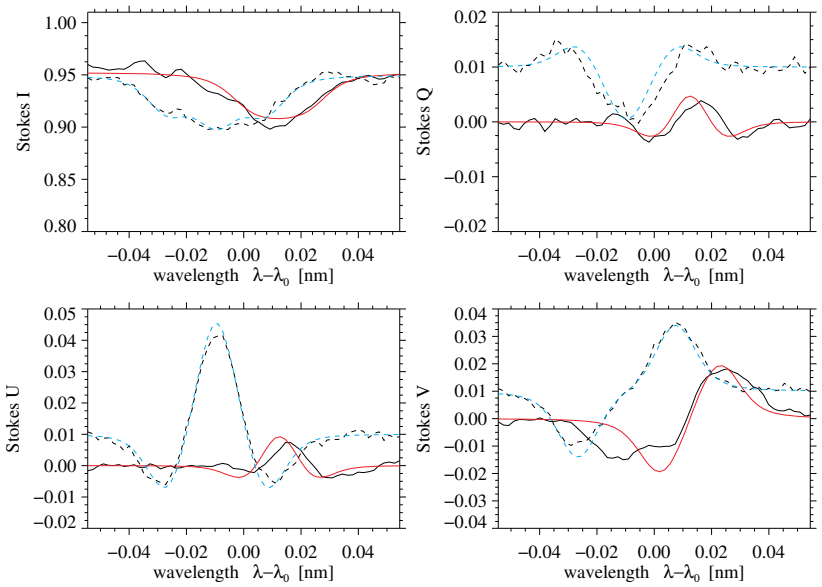

Fig. 7 The observed Ca I Stokes profiles at locations with downflows (*solid lines*) and upflows (*dashed lines*) in the penumbra of spot S2, respectively (see "+" signs in Fig. 5). The SIR results for these profiles are depicted in light blue (upflow) and red (downflow) colors. All dashed curves are shifted upwards by 0.01 for clarity.

is visible. A conspicuous patch of redshifts is located at the southerly penumbra of spot S1, whereas blueshifts can be seen in the northerly penumbra of spot S2. On the lower-right of spot S2 (42″, 18″) a small region with blueshifts on the left and redshifts on the right is seen. This region belongs to the outer tip of a penumbral filament. However, on the upper-right of the S2 penumbra (40″, 27″), a patch with redshifts and blueshifts can be seen. These locations with red and blueshifts in close proximity likely belong to regions with flux emergence.

The maps depicting the LOS velocity for the Si I line also show the granulation pattern but with smaller amplitudes. Smaller regions with blueshifts and redshifts at the same locations can be seen as well, but not as clearly as in the lower photosphere. In the chromospheric He I LOS velocity map convective velocity patterns cannot be seen anymore. Instead the FOV is filled with some blueshifts in the lower half and redshifts in the upper half. The chromospheric velocities are much higher than in the photosphere. We do not see many filamentary structures in He I velocity map – in contrast to González Manrique et al. (2016). In the ROI all spots have the same polarity, whereas the region observed by the above authors consists of a small bipolar region, where the opposite polarities are connected by the small filaments.

3.3 Magnetic field

Since GRIS provided spectropolarimetric data, information about the magnetic field at the target location are also available. To infer the magnetic field quickly and without spending significant time on inverting the spectral lines (on the order of 10 s for each set of Stokes profiles), we created signed Stokes V, total linear polarization, and total polarization maps using the line profile for all three lines. These "quick-look'' maps are compiled in Fig. 6. The signed Stokes V maps depict positive and negative polarities. When matching the SDO images/magnetograms and the GRIS mean intensity map, it is evident that magnetic structures in the Stokes V maps closely coincide with the locations of the sunspots and pores. In all maps the sunspots have negative polarity. In the Ca I line map the lower penumbra of spot S1 appears to have positive polarity, and a smaller part of the lower S2 penumbra is also positive. This could be related to the oblique viewing geometry of this sunspot and the presumably nearly horizontal field in the penumbra. As expected, in the strong Si I line map the negative polarity is more extended and the degree of polarization is also higher. In addition, the regions of positive polarity are larger. In the maps for the He I line the upper panel is mostly negative and the lower regions have a very low positive degree of polarization. The linear polarization maps for all the lines focused on the area close to the sunspots umbrae. For the Si I line, the degree of linear polarization is highest, whereas the map for the He I line is noisier and also has the lowest value for the degree of polarization. The total polarization is present in the large areas of penumbrae and is stronger for Si I line.

The processed GRIS spectra were inverted with the SIR code developed by Ruiz Cobo & del Toro Iniesta (1992). We restricted ourselves to the photospheric Ca I λ1083.9 nm line ($g_{\rm eff}$ = 1.5) because the Si I line was place very close to the detector edge, making it difficult to properly determine the blue side of the continuum. The starting model is a single-component model, which covers the optical depth range of $-4.4 \leq \log\tau \leq +1.0$. We considered the limb-darkening factor using the equations mentioned in Pierce et al. (1977) and Pierce & Slaughter (1977). The spectral profiles were normalized to the global continuum for the inversion. A constant macro-turbulence of 1.1 cm s^{-1} was assumed and a fixed contribution of 2 % dispersed straylight was taken into consideration. The inversions of the spectra yielded the temperature stratification with three nodes. For the magnetic field strength, inclination, and azimuth as well as the

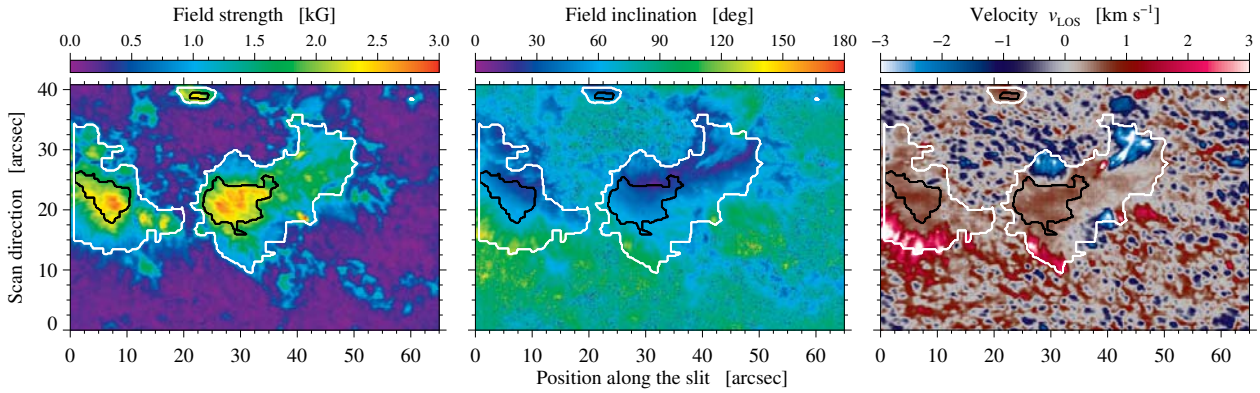

Fig. 8 Maps of physical parameters derived with the SIR code for GRIS scans taken in Ca I λ 1083.9 nm line on 2015 August 6: total magnetic field strength, magnetic field inclination, and Doppler velocity (*left to right*). The black contours mark the umbra-penumbra boundaries, where as the white contours mark the penumbra-granulation boundaries.

Doppler velocity $v_{\rm LOS}$, the calculations were carried out for one node only. Thus, these values are height-independent.

We present the observed Stokes profiles in Fig. 7 along with the profiles inverted using SIR. We chose the two locations in the FOV related to blueshifts (blue) and redshifts (red) in the penumbra of spot S2. Their positions are marked with "+" signs in Fig. 5. For both locations, SIR fits the Stokes I, Q, and U profiles well. However, the observed Stokes V for the redshift location possesses double lobes, which are not properly fitted by the one-component SIR inversion. The location, as discussed in Sect. 3.2, is likely a site of flux emergence, which leads to these peculiar Stokes V profiles. Fitting these profiles can be improved by using a two-component model in the SIR code. However, this is beyond the scope of the current work and will be presented in a forthcoming publication.

Figure 8 contains the total magnetic field strength, field inclination, and LOS velocity computed with SIR. The magnetic azimuth is also estimated. However, the presence of multiple azimuth centers and peculiar Stokes V profiles made it difficult to solve the magnetic azimuth ambiguity. Once more, this can be improved using a two-component model. In addition, we measure LOS velocities of around ± 3 km s^{-1}. The Ca I velocity map shown in Fig. 5 and the map derived with the SIR code are very similar. Granulation is visible in both maps. In addition, the small patch with blueshifts and redshifts on the edge of the S2 penumbra is also present.

4 Conclusions

We presented one of the data sets taken during the coordinated observing campaign at the GREGOR solar telescope in August 2015. The high-resolution spectra of active region NOAA 12396 captured with GRIS allowed us to study the flow and magnetic field properties of the trailing part of the region. SDO/HMI and IRIS images allowed to visualize the whole active region NOAA 12396 and revealed its structural complexity. HMI continuum images as well as magnetograms for the whole disk passage allowed us an insight into the temporal evolution of the observed region. They revealed constant changes in the appearance of the trailing part of the active region, especially concerning the evolution of sunspot penumbrae. The finding of Schlichenmaier et al. (2010b) stating that a steady penumbra is prevented from forming in regions of ongoing flux emergence is compatible with the behavior of active region NOAA 12396 as well. Flux emergence hindering the formation of a stable penumbra was more recently seen by Romano et al. (2013) as well.

Full Stokes polarimetry from GRIS provided the photospheric and chromospheric line core intensities, LOS velocities, and magnetic field information for the region. The photospheric line core intensity and velocity maps created using Ca I and Si I lines show the granulation pattern, which are not present in the chromospheric counter part. The larger aperture of the GREGOR solar telescope has significantly improved the spatial resolution of the magnetic field observations – as compared to observations with the same camera and polarimeter at the Vacuum Tower Telescope (VTT). In addition, the dark filamentary structures, present in He I velocity maps presented by González Manrique et al. (2016) and Balthasar et al. (2016), are not seen for the current region because the ROI only encompasses the trailing spots of the same polarity instead of a bipolar region. The magnetic field information was extracted by combining "quick-look" maps (degree of polarization and LOS velocity) with results from the SIR code for the Ca I line. Single-component inversions are in some case simplistic because of double lobes in the Stokes V profiles. Results from two-components inversions with SIR are deferred to a forthcoming publication.

In current study, we showed the potential of coordinated campaigns combining multiple telescope and instruments both on the ground and from space. The next step will be to study the relationship between chromospheric and photospheric fields in more detail. Similar coordinated campaigns are scheduled for upcoming observing seasons, where we expect a better temporal coverage for the high-resolution

observations by including the Dunn Solar Telescope (DST) and New Solar Telescope (NST). Thus, we have a perfect combination of high-resolution and synoptic observations targeting the complexity of sunspots and their fine structure with the aim to gain a more complete and deeper understanding of the underlying physical processes.

Acknowledgements. The 1.5-meter GREGOR solar telescope was built by a German consortium under the leadership of the Kiepenheuer-Institut für Sonnenphysik in Freiburg with the Leibniz-Institut für Astrophysik Potsdam, the Institut für Astrophysik Göttingen, and the Max-Planck-Institut für Sonnensystemforschung in Göttingen as partners, and with contributions by the Instituto de Astrofísica de Canarias and the Astronomical Institute of the Academy of Sciences of the Czech Republic. SDO HMI and AIA data are provided by the Joint Science Operations Center – Science Data Processing. MS is supported by the Czech Science Foundation under the grant 14-0338S. CD is supported by the German Science Foundation (DFG) under grant DE 787/3-1. This study is supported by the European Commission's FP7 Capacities Programme under the Grant Agreement number 312495. SJGM is grateful for financial support from the Leibniz Graduate School for Quantitative Spectroscopy in Astrophysics, a joint project of AIP and the Institute of Physics and Astronomy of the University of Potsdam (UP).

References

Avrett, E. H., Fontenla, J. M., & Loeser, R. 1994, in Infrared Solar Physics, eds. D. M. Rabin, J. T. Jefferies, & C. Lindsey, IAU Symp., Vol. 154, 35
Balthasar, H., Beck, C., Gömöry, P., et al. 2013, Centr. Eur. Astrophys. Bull., 37, 435
Balthasar, H., Gömöry, P., González Manrique, S. J., et al. 2016, AN, submitted
Borrero, J. M., & Ichimoto, K. 2011, Liv. Rev. Solar Phy., 8, 4
Brandt, P. N., & Wöhl, H. 1982, A&A, 109, 77
Brickhouse, N. S., & Labonte, B. J. 1988, Sol. Phys., 115, 43
Cheung, M. C. M., Rempel, M., Title, A. M., & Schüssler, M. 2010, ApJ, 720, 233
Collados, M. 1999, in Third Advances in Solar Physics Euroconference: Magnetic Fields and Oscillations, eds. B. Schmieder, A. Hofmann, & J. Staude, ASP Conf. Ser., Vol. 184, 3
Collados, M., Lagg, A., Díaz García, J. J., et al. 2007, in The Physics of Chromospheric Plasmas, eds. P. Heinzel, I. Dorotovič, & R. J. Rutten, ASP Conf. Ser., Vol. 368, 611
Collados, M., López, R., Páez, E., et al. 2012, AN, 333, 872
Couvidat, S., Schou, J., Shine, R. A., et al. 2012, Sol. Phys., 275, 285
De Pontieu, B., Title, A. M., Lemen, J. R., et al. 2014, Sol. Phys., 289, 2733
Del Toro Iniesta, J. C. 1996, Vistas Astron., 40, 241
Denker, C., von der Lühe, O., Feller, A., et al. 2012, AN, 333, 810
Dere, K. P., Schmieder, B., & Alissandrakis, C. E. 1990, A&A, 233, 207
Evershed, J. 1909, MNRAS, 69, 454
Gallagher, P. T., Moon, Y.-J., & Wang, H. 2002, Sol. Phys., 209, 171
González Manrique, S. J., Kuckein, C., Pastor Yabar, A., et al. 2016, AN, submitted
Hale, G. E. 1908, ApJ, 28, 315
Hofmann, A., Arlt, K., Balthasar, H., et al. 2012, AN, 333, 854
Kuckein, C., Martínez Pillet, V., & Centeno, R. 2012, A&A, 539, A131
Lemen, J. R., Title, A. M., Akin, D. J., et al. 2012, Sol. Phys., 275, 17
Montesinos, B., & Thomas, J. H. 1997, Nature, 390, 485
Pierce, A. K., & Slaughter, C. D. 1977, Sol. Phys., 51, 25
Pierce, A. K., Slaughter, C. D., & Weinberger, D. 1977, Sol. Phys., 52, 179
Rempel, M., & Cheung, M. C. M. 2014, ApJ, 785, 90
Rezaei, R., Bello González, N., & Schlichenmaier, R. 2012, A&A, 537, A19
Rimmele, T. R. 1995, ApJ, 445, 511
Rimmele, T. R., & Marino, J. 2006, ApJ, 646, 593
Romano, P., Frasca, D., Guglielmino, S. L., et al. 2013, ApJ, 771, L3
Rüedi, I., Solanki, S. K., & Livingston, W. C. 1995, A&A, 293, 252
Ruiz Cobo, B., & del Toro Iniesta, J. C. 1992, ApJ, 398, 375
Scharmer, G. B., Gudiksen, B. V., Kiselman, D., Löfdahl, M. G., & Rouppe van der Voort, L. H. M. 2002, Nature, 420, 151
Scherrer, P. H., Schou, J., Bush, R. I., et al. 2012, Sol. Phys., 275, 207
Schlichenmaier, R. 2002, AN, 323, 303
Schlichenmaier, R., Bello González, N., Rezaei, R., & Waldmann, T. A. 2010a, AN, 331, 563
Schlichenmaier, R., & Collados, M. 2002, A&A, 381, 668
Schlichenmaier, R., Jahn, K., & Schmidt, H. U. 1998a, ApJ, 493, L121
Schlichenmaier, R., Jahn, K., & Schmidt, H. U. 1998b, A&A, 337, 897
Schlichenmaier, R., Rezaei, R., Bello González, N., & Waldmann, T. A. 2010b, A&A, 512, L1
Schmidt, W., Stix, M., & Wöhl, H. 1999, A&A, 346, 633
Schmidt, W., von der Lühe, O., Volkmer, R., et al. 2012, AN, 333, 796
Schou, J., Scherrer, P. H., Bush, R. I., et al. 2012, Sol. Phys., 275, 229
Solanki, S. K. 2003, A&A Rev., 11, 153
Spruit, H. C. & Scharmer, G. B. 2006, A&A, 447, 343
Swensson, J. W., Benedict, W. S., Delbouille, L., & Roland, G. 1970, Memo. Soc. R. Sci. Liége, 5
Tiwari, S. K., van Noort, M., Solanki, S. K., & Lagg, A. 2015, A&A, 583, A119
Tritschler, A., Schlichenmaier, R., Bellot Rubio, L. R., Berkefeld, T., & Schelenz, T. 2004, A&A, 415, 717
Trujillo Bueno, J., Landi Degl'Innocenti, E., Collados, M., Merenda, L., & Manso Sainz, R. 2002, Nature, 415, 403
Wachter, R., Schou, J., Rabello-Soares, M. C., et al. 2012, Sol. Phys., 275, 261
Wallace, L., Livingston, W., Hinkle, K., & Bernath, P. 1996, ApJS, 106, 165
Westendorp Plaza, C., del Toro Iniesta, J. C., Ruiz Cobo, B., et al. 1997, Nature, 389, 47

